Cell

Polony gels enable amplifiable DNA stamping and spatial transcriptomics of chronic pain

Graphical abstract

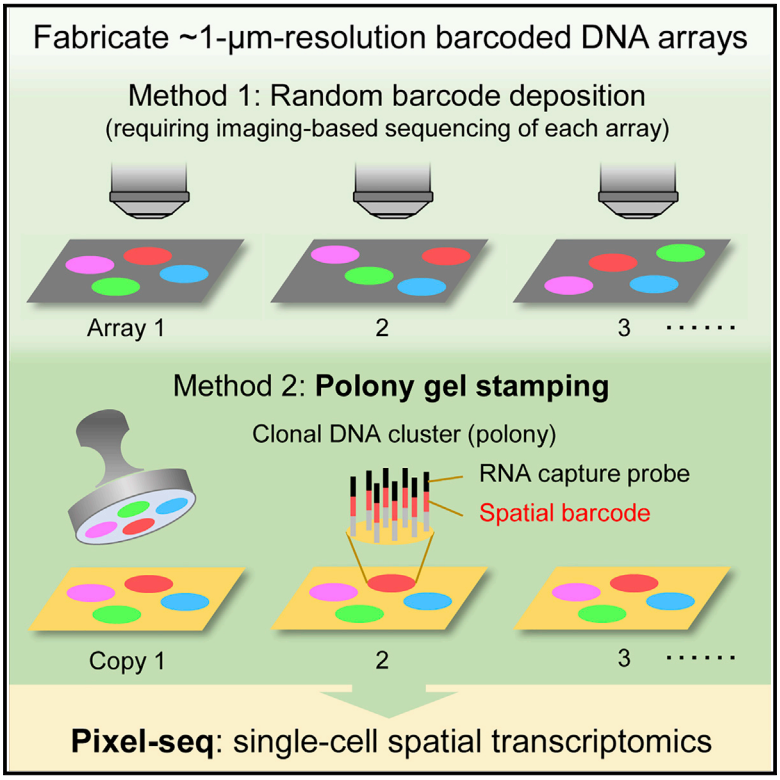

Highlights

- Polony gel stamping enables vastly scalable replication of DNA cluster arrays
- Polony gels capture tissue RNAs with high spatial resolution and efficiency
- Pixel-seq spatially maps single-cell transcriptomes of mouse brain tissues
- Pixel-seq reveals chronic pain-induced changes in the parabrachial nucleus

Authors

Xiaonan Fu, Li Sun, Runze Dong, ..., Shin Lin, Richard D. Palmiter, Liangcai Gu

Correspondence

gulc@uw.edu

In brief

Polony gels, arrays of ~1-micron-sized DNA clusters bearing unique barcodes, enable repeatable, gel-to-gel array replication and *in situ* capture of tissue RNAs with high resolution and efficiency. Pixel-seq, a polony gel-based, single-cell spatial transcriptomic assay, reveals neuronal and glial heterogeneity and chronic pain-induced changes in the mouse parabrachial nucleus.

Fu et al., 2022, Cell *185*, 4621–4633
November 23, 2022
https://doi.org/10.1016/j.cell.2022.10.021

CellPress

Cell

CellPress

Resource

Polony gels enable amplifiable DNA stamping and spatial transcriptomics of chronic pain

Xiaonan Fu,[1,2,9] Li Sun,[1,2,3,9] Runze Dong,[1,2,4,9] Jane Y. Chen,[1,5] Runglawan Silakit,[1,6] Logan F. Condon,[1,5,7] Yiing Lin,[8] Shin Lin,[6] Richard D. Palmiter,[1,5] and Liangcai Gu[1,2,10,*]

[1]Department of Biochemistry, University of Washington, Seattle, WA 98195, USA
[2]Institute for Protein Design, University of Washington, Seattle, WA 98195, USA
[3]TopoGene Inc., Seattle, WA 98195, USA
[4]Graduate Program in Biological Physics, Structure and Design, University of Washington, Seattle, WA, USA
[5]Howard Hughes Medical Institute, University of Washington, Seattle, WA 98195, USA
[6]Division of Cardiology, Department of Medicine, University of Washington, Seattle, WA 98195, USA
[7]Graduate Programs in Medical Scientist Training and Neuroscience, University of Washington, Seattle, WA, USA
[8]Department of Surgery, Washington University School of Medicine, St. Louis, MO 63110, USA
[9]These authors contributed equally
[10]Lead contact
*Correspondence: gulc@uw.edu
https://doi.org/10.1016/j.cell.2022.10.021

SUMMARY

Methods for acquiring spatially resolved omics data from complex tissues use barcoded DNA arrays of low- to sub-micrometer features to achieve single-cell resolution. However, fabricating such arrays (randomly assembled beads, DNA nanoballs, or clusters) requires sequencing barcodes in each array, limiting cost-effectiveness and throughput. Here, we describe a vastly scalable stamping method to fabricate polony gels, arrays of ~1-micrometer clonal DNA clusters bearing unique barcodes. By enabling repeatable enzymatic replication of barcode-patterned gels, this method, compared with the sequencing-dependent array fabrication, reduced cost by at least 35-fold and time to approximately 7 h. The gel stamping was implemented with a simple robotic arm and off-the-shelf reagents. We leveraged the resolution and RNA capture efficiency of polony gels to develop Pixel-seq, a single-cell spatial transcriptomic assay, and applied it to map the mouse parabrachial nucleus and analyze changes in neuropathic pain-regulated transcriptomes and cell-cell communication after nerve ligation.

INTRODUCTION

Spatially barcoded DNA arrays are increasingly used for *in situ* capture and sequencing of RNAs and proteins to map the structure and function of heterogeneous tissues (Chen et al., 2022; Cho et al., 2021; Rodriques et al., 2019; Stahl et al., 2016; Stickels et al., 2021; Vickovic et al., 2019, 2022). To achieve single-cell resolution, DNA arrays require features significantly smaller than cells to delineate different shapes. Traditional spotting (DeRisi et al., 1996; Schena et al., 1995) or light-directed synthesis (Fodor et al., 1991) methods for the deposition or *in situ* synthesis of sequence-defined oligonucleotides at specific array positions on a substrate often generate features larger than mammalian cells (>10 μm) with significant gaps to prevent feature merging. Recent advances of spatial transcriptomics utilized random arrays of smaller features such as DNA-coated beads (Rodriques et al., 2019; Vickovic et al., 2019), DNA nanoballs (Chen et al., 2022), and polymerase colonies (known as polonies [Gu et al., 2014] or DNA clusters [Cho et al., 2021]), all requiring decoding feature barcodes by sequencing each array in specialized flowcells. The barcode sequencing is a major cost- and rate-limiting factor of scaling up the array production; for example, sequencing barcodes in 38 tiles of 0.8 mm^2 in an Illumina MiSeq flowcell (Cho et al., 2021) added a cost of ~$30 per mm^2 and a time of 3–4 h per run, scaling linearly with barcode length and array size. It is desirable to develop sequencing-independent fabrication, which requires a paradigm shift in our underlying approach.

A possible method for simple and fast array fabrication is microcontact printing (Xia and Whitesides, 1998) using an elastomeric stamp to simultaneously copy arrayed molecules to a substrate. However, it has been an unsolved problem to construct a barcoded array on a stamp allowing consecutive printing without progressive decline of feature resolution and printed DNA amounts. Here, we report that polonies formed on the surface of an elastomeric, crosslinked polyacrylamide "stamp gel" as templates can be efficiently copied to many "copy gels" by DNA polymerase-catalyzed chain extension (Figure 1A). The gel-to-gel replication reliably achieved sub-micrometer resolution because all primers and templates are covalently attached

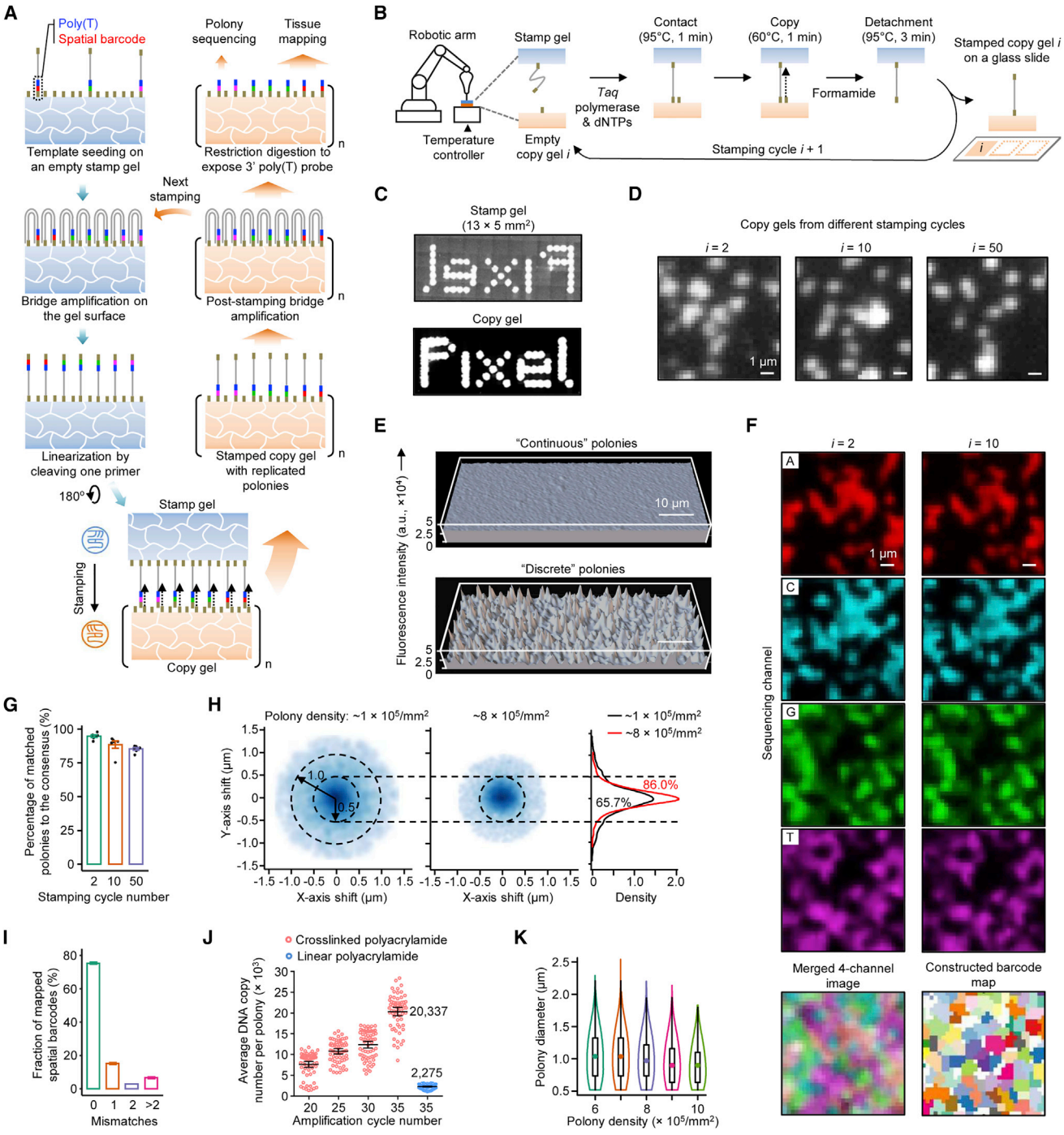

Figure 1. Fabrication and characterization of polony gels

(A) Schematic of the amplifiable DNA stamping. USER-linearized single-stranded polonies are copied from a stamp to many copy gels. Copied DNAs are further bridge-amplified to complete the replication. A few copy gels are used as the stamp for next fabrication or for polony sequencing to create a spatial barcode map; the majority are used for tissue mapping assays.

(B) A gel-to-gel DNA copying process automated with a stamping device.

(C) Millimeter-scale images of SYBR Green-stained polonies in a stamp and a copy gels. For comparison, templates were seeded on the masked, ~40-μm-thick stamp gel and amplified to polonies showing a pattern of the word "Pixel."

(D) Images of SYBR Green-stained polonies from the second, 10th, and 50th stamping cycles. The low-density polony gels (~10^5/mm^2) were selected to facilitate visual comparison.

(E) 3D intensity profiles of SYBR Green-stained, discrete, and continuous polonies amplified from templates seeded at the same density by 35 cycles.

(legend continued on next page)

to the gels to prevent DNA diffusion. Unlike traditional stamping requiring "re-inking" a stamp for consecutive printing (Lange et al., 2004), the enzymatic replication does not consume templates on the stamp. Notably, the stamping is also facilitated by DNA bridge amplification (Bentley et al., 2008) on gel surfaces to achieve a high copying efficiency and intensify faint prints. To obtain a spatial barcode map for a series of prints, only one or a few copy gels need to be sequenced. Additionally, copy gels can serve as stamps for next fabrication rounds. By utilizing polony gels, we demonstrated polony-indexed library-sequencing (Pixel-seq) for tissue mapping with high resolution and RNA capture efficiency (e.g., a mean of ~1,000 unique molecular identifiers [UMIs]/10 × 10 μm^2 in mouse tissue).

We applied Pixel-seq to analyze the mouse parabrachial nucleus (PBN), a brain region in the pons for relaying sensory information (e.g., visceral malaise, taste, temperature, itch, and pain) to forebrain structures (Palmiter, 2018). Its heterogeneous structure and cell components remain poorly understood. By creating the first cell atlas of the PBN, we identified region-specific distributions of previously known and newly found neuron types. By precise anatomical and transcriptomic comparison of PBN neurons and glial cells, we analyzed changes in neuropathic pain-regulated gene expression and cell-cell communication in the homeostatic adult brain as important adaptations to chronic pain.

RESULTS

Polony gels enable amplifiable DNA stamping and show a continuous feature distribution

We selected the crosslinked polyacrylamide as stamp and copy gels allowing the low-pressure, conformal contact and the bridge amplification of template and copied DNAs. To automate the stamping process, a benchtop device was built with a robotic arm to position the stamp, a thermocycler to control the gel temperature, a digital balance to monitor the stamping pressure, and a fluidic system to amplify DNAs (Figures 1B and S1A). Different from previous methods that generated gel-embedded polonies (Gu et al., 2014; Mitra and Church, 1999), we amplified polonies on gel surfaces (Figure S1B) to facilitate DNA replication between gels. We first compared gels of varied thicknesses attached to different sized glass surfaces; the efficient DNA copying between large gel areas was observed at increased gel thicknesses (e.g., ≥40 μm; Figure 1C). To test reproducibility and robustness, the stamping was consecutively performed for 50 cycles. Feature patterns found on the copy gels were largely consistent (Figure 1D) and stable at varied stamping pressures (Figures S1C and S1D).

High-density polonies (≥0.6 million/mm^2) often form a continuous DNA distribution with minimal feature-to-feature gaps, distinct from those amplified in Illumina nonpatterned flowcells showing a discrete, peak-shape distribution (Figure 1E). To understand the difference, we found that polonies on gel surfaces have a faster size expansion likely due to decreased gel constraints on the bridge amplification. These polonies appear to be easily accessible to restriction digestion; 93.6% of double-stranded DNAs were digested by *Taq*I to expose a 3′ poly(T) probe (Figure S1E). For spatial transcriptomic assays, the even distribution of poly(T) probes can minimize variations in RNA capture efficiency across DNA arrays. Although polonies are connected, they intend not to interpenetrate due to a polony exclusion effect (Aach and Church, 2004). Even at a high density, their borders were clearly delineated by polony sequencing (Figure 1F). Because polonies have varied sizes and shapes, to maximize the feature resolution we developed a base-calling pipeline to determine the major barcode species in each pixel (0.325 × 0.325 μm^2) of gel images to construct a spatial barcode map (Figure S1F).

The efficient replication of polony gels requires the post-stamping bridge amplification of copied DNAs, which increases DNA densities and compensates for the inefficient copying in some gel areas. However, more amplification can cause polony size expansion and thus center drifts, and introduce errors to spatial barcodes, compromising the resolution and accuracy, respectively. To assess this issue, we quantitively compared copy gels fabricated in a consecutive stamping experiment by analyzing feature patterns in multiple gel regions. Individual gels were compared with a consensus feature map constructed from aligned images of three copy gels. The repeated stamping is robust and only lost <15% of features after 50 cycles, likely due to gradual template loss on the stamp (Figure 1G). Polony center drifts were found to decrease at a higher polony density; for example, the fraction of those below 0.5 μm increased from 65.7% at ~1 × 10^5/mm^2 to 86.0% at ~8 × 10^5/mm^2 (Figure 1H), possibly due to decreased polony sizes at the increased density. By sequencing 24-base pair spatial barcodes, 93.43 ± 0.04% of matched polonies in two gels were found with matched spatial barcodes with up to two mismatched bases (Figure 1I). Amplified polonies comprise ultra-dense capture probes; for example, the amplification yielded an average of 20,337 template copies per polony after 35 cycles, a ~9-fold increase from an Illumina method (Bentley et al., 2008) (Figures 1J, S1G, and S1H). With our sequencing imaging setup, we reliably fabricated gels with ~0.6–0.8 million features per mm^2 passing filter and a mean feature diameter of 1.07 to 0.906 μm (Figure 1K). Fabricating higher-resolution gels with

(F) Four-channel sequencing images of two high-density polony gels (~8 × 10^5/mm^2) from the second and tenth stamping cycles. A spatial barcode map was generated by the pixel-level base calling.
(G) Boxplot of the percentages of polonies in copy gels matched the consensus. Data represent means of six sampled gel positions, each found with 195–332 polonies; error bars, SD.
(H) 2D and 1D density plots of relative positions of polony centers in copy gels from the consensus. Dash circles denote center drifts of 0.5 and 1 μm. n = 4,521 and 11,441 for polonies at the low and high densities, respectively.
(I) Boxplot of barcode error rates in eluted DNAs from two copy gels detected by Illumina sequencing.
(J) Comparison of polony bridge amplification efficiencies for two gel substrates. The linear polyacrylamide coating was prepared by a reported Illumina method.
(K) Violin plot of measured diameters of polonies at different densities. n = ~0.6 to 1 million.
See also Figure S1.

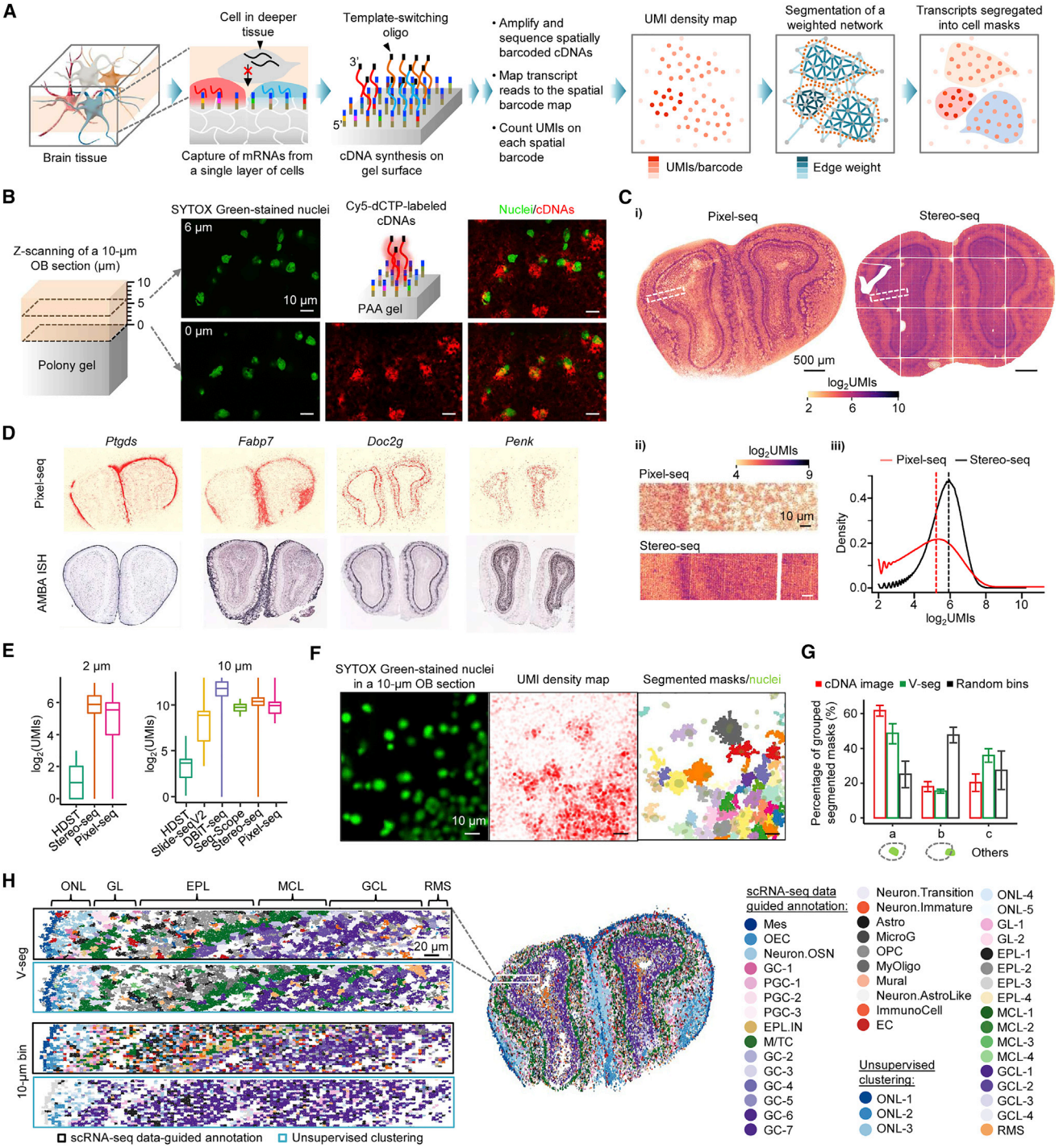

Figure 2. Pixel-seq-based single-cell spatial transcriptomics

(A) Principle of Pixel-seq. RNAs are captured from the gel-touching cell layer in a cryosectioned tissue to synthesize barcoded cDNAs with a 3′ universal sequence introduced from a template-switching oligo for cDNA amplification. cDNAs are sequenced to associate RNAs to their gel locations to create a transcript map. A k-nearest neighbor network is built on the map where each barcode represents a node. Edge weights are calculated as a function of UMI counts, the distance, and transcript similarity between two connected barcodes. The weighted network is segmented by a graph-based algorithm to create cell masks to aggregate transcripts for single-cell data analyses.

(B) Confocal analysis of stained nuclei in a mouse OB section attached to a gel and labeled cDNAs synthesized on the gel. Two detected layers of nuclei proximal (0 μm) and distal (6 μm) to the gel surface are overlaid with cDNA signals.

(legend continued on next page)

smaller and denser features is possible because even more crowded polonies still show clear boundaries (Figure S1I) but sequencing them requires improved imaging resolution.

Demonstration of single-cell spatial transcriptomics on the mouse olfactory bulb

We developed Pixel-seq (Figure 2A) with a focus on translating the 1-μm feature resolution to the single-cell resolution of the assay for complex tissues such as the brain. To test assay conditions and compare the performance, we analyzed the mouse olfactory bulb (OB) with morphologically diverse cells organized in a layered structure commonly used to validate spatial transcriptomic assays (Chen et al., 2022; Rodriques et al., 2019; Stahl et al., 2016; Stickels et al., 2021; Vickovic et al., 2019). We looked at two common issues of the array-based assays limiting the single-cell resolution, the lateral RNA diffusion between cells and the mixing of RNAs from multi-layered cells found even in thin tissue slices. The polony gel-based RNA capturing, even without tissue fixation, yielded strong cDNA signals clearly delineating boundaries of neuronal cell bodies (Figure S2A). By comparing cell sizes detected by Pixel-seq and RNAscope, the median template drift was estimated to be ~0.86 μm (Figure S2B), smaller than the average polony size, suggesting that the gel-restrained diffusion does not severely compromise the feature resolution. Of note, the gels appeared to capture tissue RNAs from a single cell layer when frozen sections were placed on the dried gels; yielded cDNA signals were colocalized with stained nuclei in the gel-contacting cells and not those in a deeper tissue (Figure 2B). The selective RNA capturing can be explained by fast occupancy of a gel surface by adjacent RNAs during the gel wetting by a tissue section (Figure S2C). The gel-based capture not only increased the resolution but also facilitated a fast preparation of cDNA sequencing libraries (~6 h; see STAR Methods).

To assess the performance, we assayed 10-μm, coronal OB sections to obtain spatially resolved transcriptomes. Specifically, in a ~13-mm^2 OB section, ~83% of raw reads were mapped to the barcode map to obtain ~82.5 million UMIs with a density range from 1 to 678 UMIs/barcode. The UMI density map displays a continuous, pixel-resolution, multi-layered structure (Figure 2C, panel i). The enlarged view shows marked density patterns rising from specific cell distributions in the ultrathin tissue layer, distinct from more even UMI distributions found by similar assays such as Stereo-seq (Figure 2C, panel ii), where RNAs released from multiple cell layers were likely captured under the assay condition. Although less RNAs were expected to be found in single than multiple cell layers, our mapped UMIs had a wider density range with a higher maximum (Figure 2C, panel iii), demonstrating the high capture efficiency. About 23,000 unique genes were detected with over 10 UMIs in at least one of three replicates; the data showed high correlation ($R \geq 0.968$; Figure S2D). Detected OB layer-specific gene expressions agree with the *in situ* hybridization (ISH) data from the Allen Mouse Brain Atlas (AMBA) (Figure 2D). Together, compared with other assays, Pixel-seq achieved the high resolution and sensitivity (Figure 2E and Table S1).

With the high-resolution transcript maps in hand, we sought to segment mapped transcripts into single cells. Our simulation with seqFISH-mapped mouse cortex data (Eng et al., 2019) suggests that the 1-μm feature resolution is sufficient to separate regular cell bodies (Figure S2E). However, it is challenging to trace all cell boundaries with standard staining methods and use the confocal images as ''references'' to guide cell segmentation. So far, array-captured brain transcripts were often randomly segregated in spatially aggregated pixels or random bins (Chen et al., 2022; Rodriques et al., 2019; Stahl et al., 2016; Stickels et al., 2021; Vickovic et al., 2019). The reference-independent segmentation is highly desirable, but available algorithms (e.g., Baysor [Petukhov et al., 2022]) were developed for imaging-based data on selected genes (Codeluppi et al., 2018; Moffitt et al., 2018) and cannot be directly applied to the global transcriptome data. Thus, we developed a volume-distance-based segmentation algorithm (V-seg) which constructs a nearest neighbor network from mapped transcripts, calculates edge weights (termed volume distances) based on UMI densities, the spatial distance and transcript similarity between two neighboring barcodes, and then segments the weighted network into masks representing single cells by a computationally efficient, graph-based community detection algorithm (Figure 2A [right three panels] and S2F).

We applied V-seg to segment the OB data, validated the results with the nuclear staining images, and compared the performance with image-based segmentation and random bins. In the OB section, V-seg segmented ~86% (~70.8 million) of mapped transcripts into 23,351 masks; 22,830 with UMIs ≥256 were selected for cell classification. Unsupervised clustering (Hao et al., 2021) of segregated transcripts recapitulated layer-specific distributions of major neuronal and non-neuronal cell types

(C) Comparison of OB UMI density maps by RNA captures from a single (Pixel-seq) and multiple layered cells (Stereo-seq). (i) Maps of total UMI densities measured on 2 × 2 μm^2 bins. (ii) Zoom-in comparison of the selected regions in (i) (white dotted boxes). (iii) Density plot of detected UMIs in 2 × 2 μm^2 bins in the whole tissues. Means (dash lines): 45.6 and 60.5; maxima: 1,979 (Pixel-seq) and 1,091 (Stereo-seq).

(D) Comparison of selected gene expressions detected by Pixel-seq and the AMBA ISH data.

(E) Comparison of the capture efficiency of Pixel-seq and recent data from similar assays (see Table S1). The Pixel-seq OB UMIs were counted on bins of 7 × 7 (2 μm) and 33 × 33 (10 μm; a cutoff of 265 UMIs) pixels.

(F) Validation of the V-seg result by overlaying segmented masks with stained nuclei in the same tissue. Immediately after placing the tissue on the gel pre-soaked with SYTOX Green, stained nuclei were imaged with the epifluorescence microscope used for polony gel sequencing.

(G) Comparison of the accuracy of V-seg, labeled cDNA image segmentation, and random bins of a size close to the average V-seg mask size. Results were validated by the colocalization with nuclei described in (F). (a) Masks containing single nuclei; (b) masks partially overlapped with single nuclei; (c) others including those overlapped with multiple or zero nuclei.

(H) Comparison of cell annotation outcomes of the segmentation by V-seg and random bins. Aggregated transcripts were analyzed by scRNA-seq data-guided annotation or unsupervised clustering. See full names of cell types in Figure S2G.

See also Figure S2.

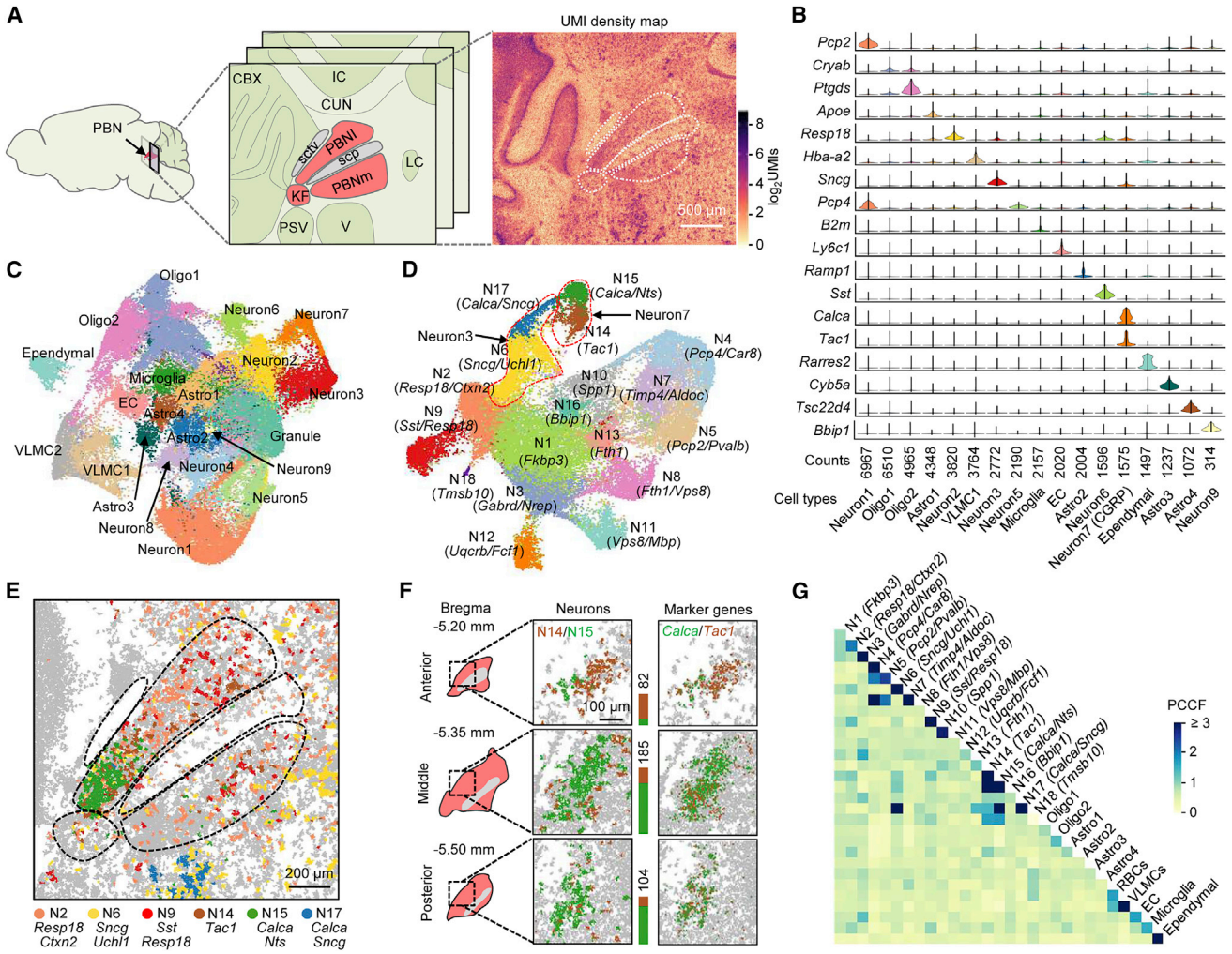

Figure 3. Single-cell spatial transcriptomic mapping of the PBN

(A) Anatomical structure and UMI density map of a middle coronal section comprising the PBN (red) and neighboring regions. PBNl, lateral PBN; PBNm, medial PBN; KF, Kölliker-Fuse subnucleus; sctv, ventral spinocerebellar tract; scp, superior cerebellar peduncle; CBX, cerebellar cortex; IC, inferior colliculus; CUN, cuneiform nucleus; PSV, principal trigeminal sensory nucleus; V, trigeminal motor nucleus; LC, locus coeruleus.

(B) Violin plots of selected top genes showing differential expression in each cluster.

(C) Uniform Manifold Approximation and Projection (UMAP) clustering of the transcripts segregated into ~60,000 masks from four middle PBN sections passing quality control metrics. Astro, astrocyte; Oligo, oligodendrocyte; EC, endothelial cell; VLMC, vascular and leptomeningeal cell.

(D) UMAP clustering of the data representing 31,505 neuronal cells isolated from (C) with defined marker gene(s) for each cluster. Dotted lines highlight examples of separated subclusters from non-separated clusters in (C).

(E) Spatial distribution of major neuronal subtypes in the PBN and V.

(F) 3D mapping of PBN *Tac1* (brown) and *Calca* (green) neurons. Stacked bars denote cell counts.

(G) Cell-cell contact heatmap of annotated clusters in (C) and (D). Cell contacts were quantified by a PCCF colocalization statistic.

See also Figure S3.

identified by single-cell RNA sequencing (scRNA-seq) (Tepe et al., 2018) (Figure S2G). To validate segmented cells, masks were aligned to stained nuclei in the same tissue (Figure 2F); to facilitate data registration, tissue images were acquired with the same microscope and magnification for the gel sequencing. Compared with random bins, V-seg and cDNA signal-guided segmentation, like the poly(A) staining-guided segmentation in other assays (Codeluppi et al., 2018; Moffitt et al., 2018), generated respectively 1.95- and 2.46-fold more masks containing a whole nucleus and 3.10- and 2.65-fold less masks partially overlapped with single nuclei (Figure 2G). About 36% of V-seg masks contained multiple or no nuclei partly because some nuclei were not in the gel-contacting cell layer (Figure 2B). The improved segmentation by V-seg is confirmed by the high similarity between the unsupervised clustering and scRNA-seq data-guided annotation results (Figure 2H), measured cell body sizes close to previous report (Pinching and Powell, 1971) (Figure S2H), and the consistency between mask shapes and marker gene

distributions (Figure S2I). Segmented cells show cell-type-specific UMI densities (Figure S2J) and their UMI counts typically increase with cell sizes; for example, the means of periglomerular type 1 (PGC-1; a mean diameter of 10.9 ± 4.6 μm) and mitral/tufted cells (M/TCs; 14.5 ± 4.8 μm) were 3,346 and 6,458 UMIs/cell, respectively. Our result reasonably agrees with the scRNA-seq data on gene expression (R = 0.722; Figure S2K) and cell type abundances (Figure S2L); the discrepancies are mostly due to the partial capture from cell pieces by Pixel-seq and cell losses in the dissociative assay.

Cell atlas of the PBN

We looked at the PBN packed with neuron clusters (or nuclei), a common structure in the brain distinct from the OB layered structure, which is hard to analyze without single-cell resolution. The PBN relays sensory information from the periphery to the forebrain, responding to internal and external stimuli, as well as maintaining homeostasis (Palmiter, 2018). Previous studies using unique genetic markers located neurons within the PBN that transmit distinct signals related to thermal sensation (Norris et al., 2021), pain (Huang et al., 2019), appetite, visceral malaise, and threat detection (Campos et al., 2018). However, the identity of most cells in the PBN and their spatial organization were unknown.

We first analyzed PBN coronal sections in the middle (bregma, −5.35 mm) with the largest cross section. With a sequencing depth of ∼88%, each section yielded 21 ± 4.5 million UMIs located to a ∼3 × 3 mm^2 region centered on the PBN surrounded by the cerebellar cortex (CBX), trigeminal motor (V) and principal sensory nuclei (PSV), locus coeruleus (LC), and cuneiform nucleus (CUN) (Figure 3A). The UMI density map allows charting PBN subregions such as the lateral (PBNl) and medial (PBNm) divided by the superior cerebellar peduncle (scp), a large fiber tract showing distinctly fewer UMIs. Mapped transcripts were aggregated into 15,618 ± 1,093 cell masks per section. Unsupervised clustering by Seurat defined distinctive marker genes (Figure 3B), which were compared to the consensus in https://mousebrain.org (Zeisel et al., 2018) to identify 21 neuronal and non-neuronal cell types (Figure 3C). Further subclustering of neurons identified 18 subtypes (Figure 3D).

To assess the robustness of the clustering, the spatial patterns of clustered cells were compared to the AMBA anatomic reference (Figure S3A). Most of clustered cells exhibit region-specific distributions correlated with the anatomical structure of the PBN and surrounding regions (Figures S3B and S3C). For example, ∼81.0 and ∼53.2% of clustered *Calca*/*Nts*$^+$ and *Tac1*$^+$ neuron subtypes were found in different subregions of the PBNl (Figure 3E), consistent with previous reports (Barik et al., 2018; Campos et al., 2018). The *Calca*$^+$ neurons in the PBN and the trigeminal region were separated by differentially expressed markers (e.g., *Sncg*); the latter were correctly segmented from mixed trigeminal motor neurons (*Sncg*/*Uchl1*$^+$) in the same region. Additionally, two unknown PBN neurons were identified: the *Resp18*/*Ctxn2*$^+$ subtype in the PBNl's dorsal and ventral subnuclei, the *Sst*/*Resp18*$^+$ in the central subnucleus, and both also in the PBNm (Figure 3E). Their locations overlap with areas involved in a taste-guided behavior (Jarvie et al., 2021). Some non-neuronal cells also show region specificity; for example, the most abundant astrocyte subtype, Astro1, was enriched in the PBN and the neighboring pontine central gray region (Figure S3B).

To study the three-dimensional (3D) heterogeneity, we analyzed the anterior, middle, and posterior sections of the same PBN sample (bregma, −5.20, −5.35, and −5.50 mm, respectively). Distinct changes along the rostral-caudal extent of the PBN were observed for distributions of major neuropeptide-expressing genes (Figure S3D) and validated by the AMBA ISH (Figure S3D) and RNAscope data (Figure S3E), implying transcriptomic and anatomical heterogeneity. We focused on the two known neuron subtypes in the same subnucleus, *Calca*/*Nts*$^+$ and *Tac1*$^+$. The clustering, as well as the spatial marker gene distributions, revealed their 3D organization: the *Tac1*$^+$ cells are densely populated in the anterior position and surround the *Calca*/*Nts*$^+$ in the middle position, and both are overlapped in the posterior position (Figure 3F).

Because the distance between cells affects their communication, we measured direct cell contacts in the PBN atlas. Adjacent cells were quantified using a pair cross-correlation function (PCCF) statistic (Philimonenko et al., 2000) to compare detected cell contacts (or colocalization) between the same or different subtypes to the probability of the random colocalization. The high colocalization between the same cell types agrees with observed cell aggregations; for example, the Purkinje (*Pcp2*/*Pvalb*$^+$) and Bergmann (*Timp4*/*Aldoc*$^+$) cells in the cerebellum and CGRP-expressing neurons (*Calca*/*Nts*$^+$) in the PBN (Figures 3G and S3C). High neuron-neuron contacts were found for the *Calca*/*Nts*$^+$ and *Tac1*$^+$ in the PBNl and the *Calca*/*Sncg*$^+$ and *Sncg*/*Uchl1*$^+$ in the trigeminal. Typically, cells showing region-specific distributions were found with preferential contacts with specific neurons or non-neuronal cells.

Cell type- and subnucleus-specific transcript changes in response to chronic pain

After having the transcriptome reference map, we sought to discover if our method could detect changes in gene expression in response to stimuli. The precise analysis of activity-triggered adaptations in specific cells requires comparison of functionally identical cells (e.g., the same cell type in identical brain regions and with similar connectivity) from different animals. To demonstrate the transcriptomic and anatomical accuracy of Pixel-seq for this application, we analyzed chronic-pain-regulated changes in the PBN. The PBN is known to be a major hub to receive, process, and relay nociceptive signals (Palmiter, 2018; Sun et al., 2020). As part of adaptations to neuropathic pain, PBN cells are likely to mount complex transcriptional responses (Yap and Greenberg, 2018). However, such changes, as well as many others in different brain regions, are yet to be unveiled.

We assayed coronal PBN sections from animals that received either a sham operation or partial sciatic nerve ligation (SNL)-induced neuropathic pain (30th day post-surgery). To facilitate comparing cells in identical anatomical sites, we divided the sections into four subregions (two PBNl and two PBNm) and the V (Figure 4A). To minimize variations caused by individual heterogeneity and the sectioning of brain samples, we focused on comparing two middle sections showing the highest cluster similarity (Figures 4B, S4A, and S4B). Unsupervised clustering of

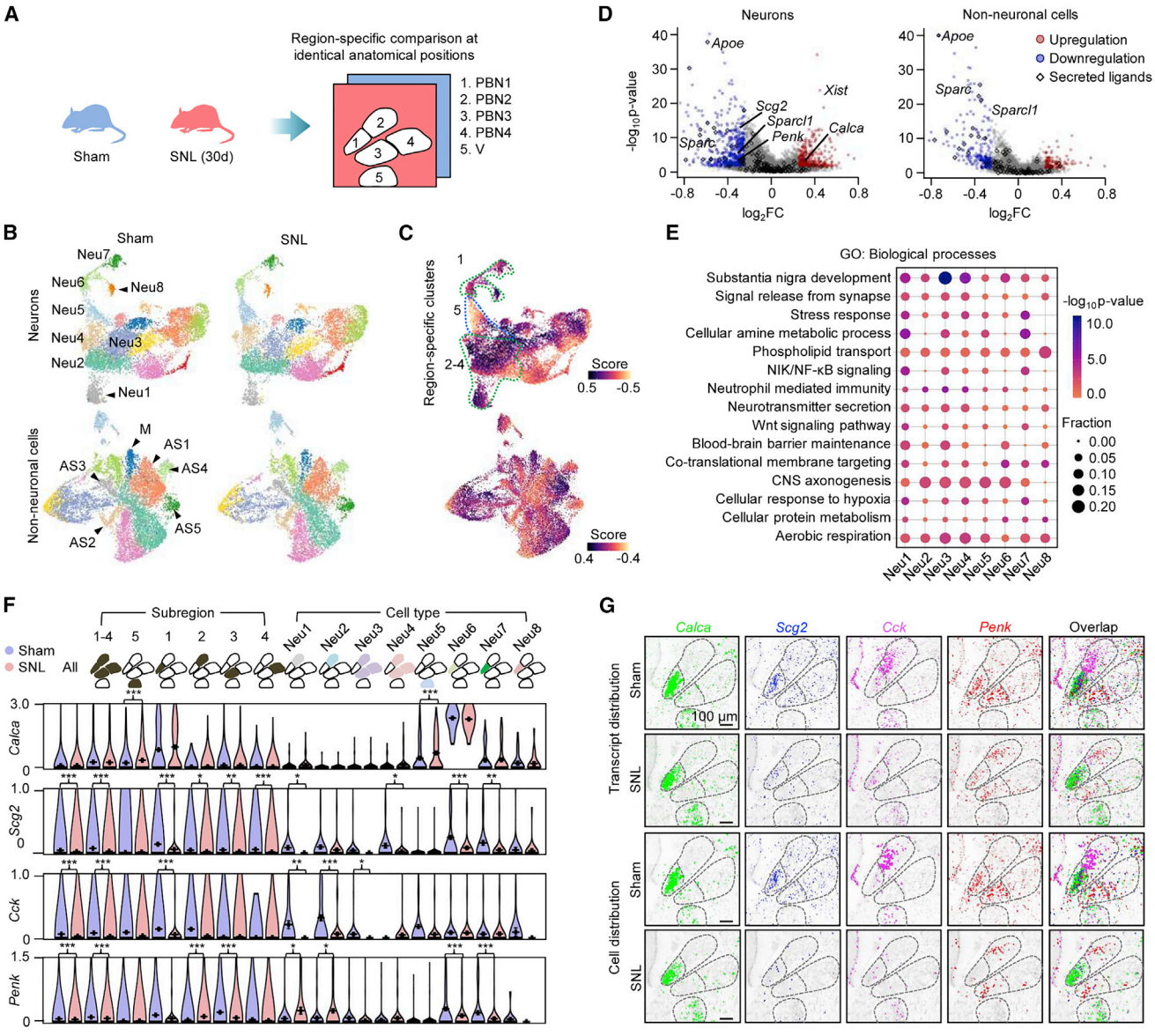

Figure 4. Chronic-pain-regulated gene expression in PBN subnuclei

(A) Comparison of the Pixel-seq data of sham and pain mice at anatomically identical PBN and V subregions. SNL (30 days), 30 days post-partial sciatic nerve ligation.

(B) UMAP analysis to compare clusters in two middle coronal PBN sections from sham and SNL mice. Segmentation data representing 15,833 neurons and 16,473 non-neuronal cells are plotted. Major neurons (Neu), astrocytes (AS), and microglia (M) in the PBN and V are labeled.

(C) Differential abundance analysis of the data in (B). Dotted lines highlight the PBN and V region-specific neuronal clusters.

(D) Differential expression analysis of the data in (B). FC, fold change. Colored genes, $|\log_2 FC| \geq 0.25$ and $p < 0.05$, Wilcoxon rank-sum test. The upregulation of *Xist* was only found in female mice.

(E) Gene Ontology (GO) enrichment analysis of differentially expressed genes in the major neuronal clusters in the PBN and V. p values, Fisher's exact test.

(F) Comparison of region- and cell-type-specific expression of major neuropeptide genes. Data represent mean values of ≥217 cells in each group; error bars, SEM. *p < 0.05, **p < 0.01, ***p < 0.001, Wilcoxon rank-sum test.

(G) Comparison of spatial patterns of the neuropeptide genes in (F) and associated cells.

See also Figure S4.

32,377 cells pooled from the two sections identified 16 neuronal and 12 non-neuronal subtypes. A differential abundance analysis (Zhao et al., 2021) of the sham and SNL mouse data detected a remarkable imbalance of cell distributions (Figure 4C), which is corroborated by changed levels and spatial patterns of individual genes (Figure S4C). Differential gene-expression analysis found 487 genes in neurons and 181 in non-neurons with altered expression, including 16 encoding secreted proteins

($p < 0.05$; Figure 4D); for example, 1.23 to 1.85-fold decreases ($p < 0.05$) of *Apoe* in glial subtypes, in contrast to the upregulation in other injury and disease models (Pfrieger and Ungerer, 2011), implying its multifaceted role in inflammation and pain modulation in the PBN. These genes in neuronal clusters were predicted to be differentially involved in neuron development, stress responses, inflammation, etc. (Figure 4E).

We next asked how genes are regulated in specific cell types within subnuclei. Of particular interest is how neuropeptide gene expression responds to the pain condition. Thus, we analyzed transcriptional changes of peptide precursor genes within the chosen PBN sections. *Calca*, the gene encoding CGRP, was slightly upregulated (1.55-fold, $p = 6.07 \times 10^{-6}$) in motor neurons in the trigeminal (Neu5), but not significantly in the PBN (Neu6) (Figures 4F and 4G). *Scg2* and *Cck* were downregulated by 2.54- and 2.82-fold ($p < 0.001$), respectively, with regional specificity: *Scg2* decreased across the PBN, but *Cck* changed mainly in the subregion 2 populated by *Resp18*/*Ctxn2*$^{+}$ neurons. Notably, *Penk*, encoding an opioid precursor, showed decreased expression in subregions 1 and 3: 2.13- and 3.03-fold, respectively ($p < 0.001$), but a 3.07-fold increase in the subregion 2 (Neu1 and Neu2; $p < 0.05$). These examples, along with all the other changes, provide valuable clues for future functional experiments.

Cell-cell communication coordinated by transcriptional dynamics of microglia and astrocytes

Given the reference and pain-induced transcriptome maps, we asked how gene regulation affects local cell-cell communication. To quantitatively compare cell-signaling networks, we computed signaling likelihoods for each cell as "sender" or "receiver" using ligand and receptor transcript levels and spatial distances from other senders and receivers (Figure S5A) (Cang and Nie, 2020). Because transcripts are mainly detected in cell bodies and it is difficult to analyze the long-distance communication mediated by cell projections, neurons and non-neuronal cells were treated equally in this analysis. The comparison of signaling likelihoods between the sham and SNL mouse datasets indicates that the major changes in the PBN region were associated with microglia and astrocytes (Figure S5B) known to coordinate neuronal development and homeostasis (Vainchtein and Molofsky, 2020). A subcluster-level analysis of signaling between microglia (M), astrocytes (AS1–AS5), and major PBN neuron subtypes (N1–N4 and N6–N8) revealed subcluster-specific increases or decreases in microglial and astrocyte signaling likelihoods (Figure 5A). A detailed comparison of the contributions by individual ligand-receptor(s) pairs found that top contributors are neuropeptides, cytokines, glycoproteins, lipoproteins, and their receptors (Figure 5B). Furthermore, to understand the signaling heterogeneity, cells of a sender subcluster were profiled for the contribution by each ligand. Interestingly, the senders showed a bimodal (e.g., *Mif* in N2 and *Apoe* in AS1) or unimodal distribution (e.g., *Spp1* in N3 and *C1qb* in M), and the pain-responsive and non-responsive subpopulations appeared to be separated in the bimodal distribution where the responsive cells had higher signaling likelihoods than the non-responsive (Figure 5C).

Given the signaling importance of microglia and astrocytes, we further investigated their transcriptomic heterogeneity. To date, microglial heterogeneity associated with physiologic roles, such as supporting synaptic development and remodeling in the homeostatic adult brain, is yet to be confirmed by scRNA-seq (Li et al., 2019) because microglial gene regulation is environmentally sensitive and can be easily disrupted by tissue dissociation (Gosselin et al., 2017). Here, 584 cells with microglial markers (e.g., *C1qa* and *C1qb*) were re-clustered into two subtypes, M1 and M1* (Figure 5D [left] and S5C). Despite their similarity, M1* was annotated with specific immune response-regulating marker genes (e.g., *Mif* and *Sod1*) involved in an interleukin-12 (Il-12)-mediated signaling pathway ($p = 6.68 \times 10^{-5}$) and neutrophil-mediated immunity ($p = 5.22 \times 10^{-4}$) (Figure S5D). M1* is different from an activated neuroinflammatory state induced by lipopolysaccharide (Liddelow et al., 2017) due to the lack of three marker genes, *Il1a*, *Tnf*, and *C1q*. Considering a strong association between their marker genes in immune regulation, M1* could represent a transition state to the activated microglia. Under the pain condition, M1* decreased from 33.6% to 22.0% of the microglial population (Figure 5D [right]). Given the different ligand and receptor profiles of M1 and M1*, the decrease of M1* is associated with the changed communication in the signaling networks. Microglia showed a relatively even spatial distribution (Figure 5E) likely due to their high motility in the tissue.

Likewise, we sought to correlate transcriptomic and signaling heterogeneity of astrocytes identified from the initial clustering. 4,471 cells were re-clustered into eight subtypes annotated with marker genes (Figures 5F and S5E); most of the subclusters are connected, suggesting a continuum of transcriptomic states. As expected, some subtypes had region-specific distributions (Figure S5F). In the clustering outcome, the pain-induced major changes were found in the subtypes 2 and 3, which is supported by the differential abundance analysis (Figure 5G [left]). To understand the transcriptomic changes, we analyzed the pseudo-temporal ordering of all subtypes (Figure 5G [right]). Projection of the whole-cell population along a pseudotime trajectory revealed three separated groups, A1, A2, and Pan (Figure 5H), which can be correlated with three astrocyte states with specific physiological roles (Liddelow et al., 2017). For example, A1 and A2 astrocytes with differentially expressed *Sparc* and *Sparcl1* are known to have destructive and protective roles, respectively, in maintaining homeostasis; thus, the increase of A1 is often associated with neuroinflammation. Here, a significant decrease of A1, mainly contributed by the subtypes 2 and 3, was found for the SNL condition ($p = 1.20 \times 10^{-7}$), suggesting that pain adaptation might involve an unknown neuronal protection mechanism. Remarkably, the comparison of astrocyte spatial distributions found that the A1 decrease was mostly in the PBN region, but the other two states had no obvious changes (Figure 5I). These results, together with the neuron-glia communication, provide important evidence of the region-specific glial transcriptomic dynamics supporting local neuronal activities.

DISCUSSION

Amplifying polonies atop crosslinked polyacrylamide gels brings advantages to the fabrication and application. The gel compatibility with microcontact printing and bridge amplification enabled

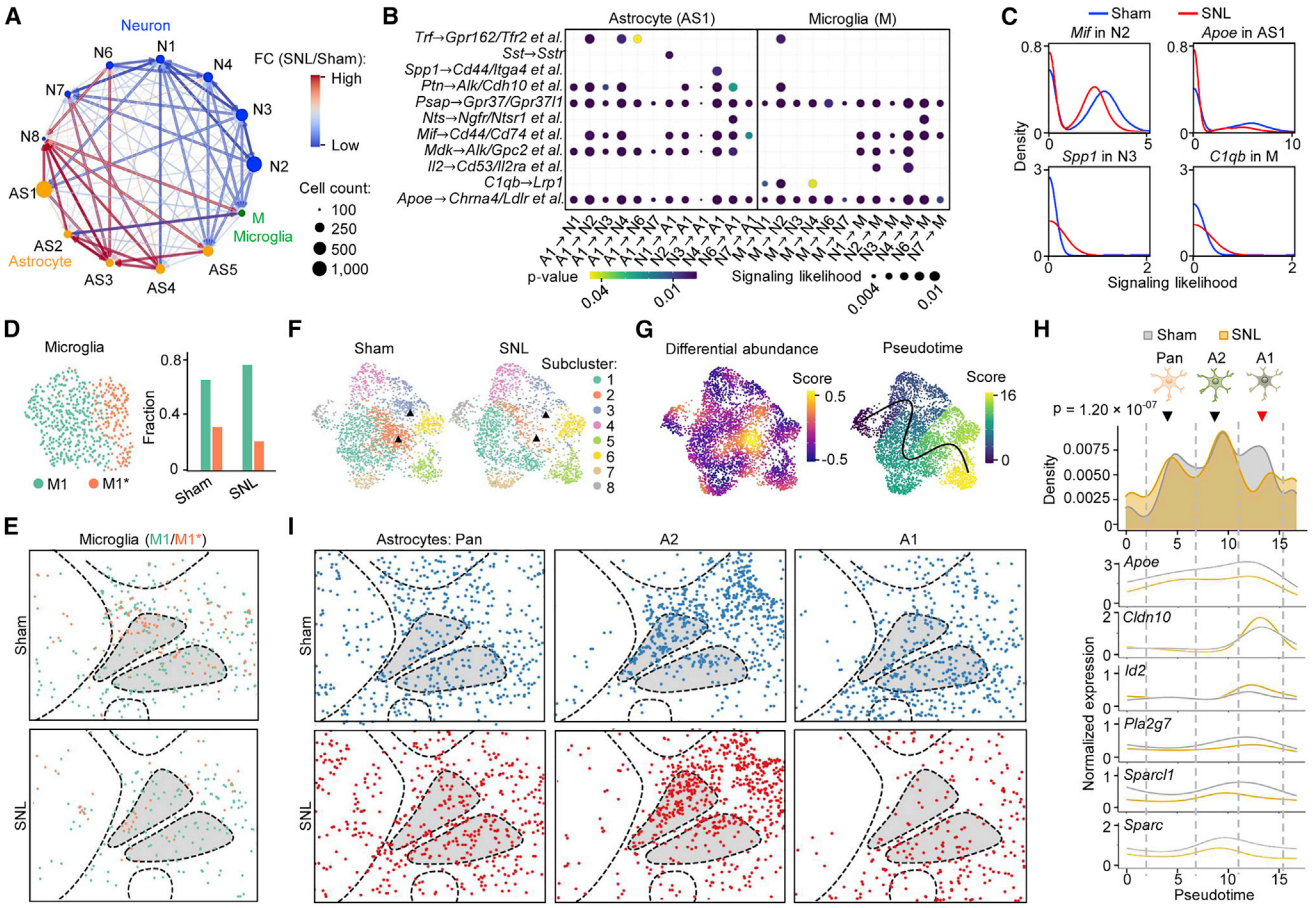

Figure 5. Chronic-pain-associated cell-cell communication and glial transcriptome dynamics

(A) Network representation of cell signaling likelihood changes for major neuronal, astrocyte, and microglial clusters with significant distributions in the PBN. Signaling likelihoods were calculated by SpaOTsc.

(B) Dot plots of contributions of paired ligand-receptor genes to the changed signaling likelihoods in (A) in the most abundant astrocyte subtype (AS1) and microglia (M). p-value, Kolmogorov-Smirnov (KS) test.

(C) Density plots of signaling likelihoods of selected ligand genes in sender clusters.

(D) UMAP analysis of the microglia and the subtype proportions under the sham and pain conditions.

(E) Spatial distribution of the microglial subclusters. Segmentation data representing 584 cells are plotted.

(F) UMAP clustering of the astrocytes under the sham and pain conditions. Segmentation data representing 4,471 cells are plotted. Triangles denote the subclusters 2 and 3 showing the most significant changes.

(G) Differential abundance (left) and pseudotime (right) analyses of the data in (F). A pseudotime trajectory was inferred by Slingshot.

(H) Density plots of astrocyte subpopulations and the normalized expression of selected genes along the pseudotime trajectory in (G). p-value, KS test.

(I) Spatial patterns of the astrocyte subpopulations.

See also Figure S5.

the submicron-resolution polony replication, reducing the fabrication cost and time. For example, the consumable cost of fabricating a 7 × 7 mm^2 array of >30 million unique features decreased to ~$3 ($0.06/mm^2; Table S2), a drastic reduction from those reported for DNA cluster and nanoball arrays (Table S3), and the time to ~7 h (see STAR Methods). Unlike similar assays (Chen et al., 2022; Cho et al., 2021) whose major cost components were array costs, our assay cost is mainly determined by the commercial sequencing of barcoded cDNA libraries (e.g., mapping a 1-mm^2 mouse brain area required ~20 million reads, a cost of ~$60 using an Illumina NovaSeq S4 flowcell). By lifting the burden of sequencing each array anew, the gel replication opens opportunities to break existing limitations. The sequencing requires placing DNAs in flowcells comprising glass or silicon surfaces suitable for optical scanning. Without the sequencing need, polony gels can be casted on other substrates for expanded assay flexibility. Gels with overly dense polonies (known as "overclustering"), which could improve the feature resolution but so far cannot be correctly sequenced, might become useful by copying different stamping gels with lower-density barcodes to the same copy gel. Finally, given the demonstrated sensitivity and resolution, crosslinked gels offer an ideal substrate for capturing tissue molecules. Their penetrable hydrophilic matrix appears to increase accessibility of densely

patterned probes to tissue targets in a diffusion-constrained environment.

Pain, a multidimensional experience, involves sensory, affective, and cognitive components in the periphery and brain. So far, single-cell transcriptomics of pain-induced changes have been limited to sensory tissues, such as dorsal root ganglion (Kupari et al., 2021), but cells and responses in other components in pain processing are largely unknown. Despite the importance in elucidating pain mechanisms and developing new analgesics, research in this field has been hampered by the lack of suitable tools. In this regard, Pixel-seq directly addresses the unmet need. The first single-cell PBN atlas and the unveiled pain-regulated changes in the spatially resolved transcriptomes provide a basis for future mechanistic studies on the PBN's roles in affective motivational and sensory discriminative pathways of pain and other processes. Although limited samples were analyzed, the unusual heterogeneity revealed by Pixel-seq highlights the necessity to analyze more anatomical positions at different time points to develop a complete view of the structural and functional landscape.

LIMITATIONS OF THE STUDY

Due the timing of developing the stamping method, the OB and PBN data were collected with sequenced gels. Despite the improved feature resolution, DNA array-based spatial transcriptomic assays still face challenges to reliably achieve single-cell resolution. Comparing our clustering results with those on dissociative scRNA-seq of brain tissues, Pixel-seq showed less optimal cell type separation. A major reason is that the feature resolution is insufficient to delineate small cell projections densely intertwined with brain cells. The reported highest feature resolution (0.22 μm; Table S1) probably reaching the limit of current array fabrication is still not enough for tracing axons and dendrites. Thus, alternative strategies such as tissue expansion (Chen et al., 2015) might be explored to push the resolution limit. In our data processing, decreased accuracy of V-seg was often found for closely aggregated cells, especially of small sizes. Better accuracy could be achieved by machine learning-based algorithms (He et al., 2021; Littman et al., 2021; Park et al., 2021; Petukhov et al., 2022) and coupling the RNA data to cell boundary signals detected with fluorescently labeled or DNA-tagged affinity reagents. In this work, polony gels were only used for capturing RNA, but they should be applicable to protein detection with DNA-tagged antibodies (Liu et al., 2020; Vickovic et al., 2022) and possibly small-molecule analytes via affinity reagent innovation (Kang et al., 2019). They can also be designed with various probes for classical DNA array-based applications (Bumgarner, 2013). Pixel-seq detected subcellular transcript distributions in brain cells, which were not further investigated in our study. Fully exploiting the 1-μm spatial resolution requires improved data analysis and validation and should be critical to revealing subcellular heterogeneity, such as protein localization, interaction, and modification.

STAR★METHODS

Detailed methods are provided in the online version of this paper and include the following:

- KEY RESOURCES TABLE
- RESOURCE AVAILABILITY
  - Lead contact
  - Materials availability
  - Data and code availability
- EXPERIMENTAL MODEL AND SUBJECT DETAILS
  - Animal
- METHOD DETAILS
  - Polony template construction
  - Gel casting
  - Primer grafting
  - Preparation of stamp gels
  - Gel stamping
  - Post-stamping gel processing
  - Polony sequencing
  - Tissue preparation for Pixel-seq
  - Transcript capturing and cDNA synthesis
  - Tissue cleanup
  - Library construction and sequencing
  - Nerve ligation surgery
  - RNAscope
  - Lateral diffusion analysis
- QUANTIFICATION AND STATISTICAL ANALYSIS
  - Polony image analysis
  - Base calling of polony sequencing
  - Transcript mapping
  - Transcript segmentation
  - Segmentation validation
  - Clustering analysis
  - scRNA-seq-guided annotation
  - Differential abundance analysis
  - Spatial pattern gene analysis
  - PCCF statistic
  - Pseudotime analysis
  - Cell-cell communication

SUPPLEMENTAL INFORMATION

Supplemental information can be found online at https://doi.org/10.1016/j.cell.2022.10.021.

ACKNOWLEDGMENTS

We thank B. Wang and W. Liang for contributions to a base calling algorithm, D. Liu and J. Cheng for the help to build the polony sequencer, Q. Tang for sharing mouse tissues, and S. Kang for discussing assay development. This work was supported by a University of Washington startup fund to L.G. and National Institutes of Health grants (R35GM128918, UG3CA268096, R21DA051555, and R21DA051194 to L.G., R41MH130299 to L.S., and R01DA024908 to R.D.P.).

AUTHOR CONTRIBUTIONS

L.G. conceived the methodology and supervised this project. L.S. and L.G. developed the polony stamping. X.F., L.G., and L.S. developed the Pixel-seq assay. L.S. and R.S. fabricated polony gels. X.F., R.D., L.G., S.Y., and Y.L. analyzed the data. J.Y.C., L.F.C., and R.D.P. designed the PBN study and prepared the tissues. L.G., X.F., and R.D. wrote the manuscript with input from other co-authors.

DECLARATION OF INTERESTS

Two patents on polony gel stamping and Pixel-seq have been filed by the University of Washington and TopoGene Inc. L.G. and L.S. are co-founders of TopoGene, which aims to commercialize polony gels.

Received: June 21, 2022
Revised: September 6, 2022
Accepted: October 18, 2022
Published: November 10, 2022

REFERENCES

Aach, J., and Church, G.M. (2004). Mathematical models of diffusion-constrained polymerase chain reactions: basis of high-throughput nucleic acid assays and simple self-organizing systems. J. Theor. Biol. *228*, 31–46. https://doi.org/10.1016/j.jtbi.2003.12.003.

Barik, A., Thompson, J.H., Seltzer, M., Ghitani, N., and Chesler, A.T. (2018). A brainstem-spinal circuit controlling nocifensive behavior. Neuron *100*, 1491–1503.e3. https://doi.org/10.1016/j.neuron.2018.10.037.

Bentley, D.R., Balasubramanian, S., Swerdlow, H.P., Smith, G.P., Milton, J., Brown, C.G., Hall, K.P., Evers, D.J., Barnes, C.L., Bignell, H.R., et al. (2008). Accurate whole human genome sequencing using reversible terminator chemistry. Nature *456*, 53–59. https://doi.org/10.1038/nature07517.

Bumgarner, R. (2013). Overview of DNA microarrays: types, applications, and their future. Curr. Protoc. Mol. Biol. *101*, 22. 22.1.11.

Campos, C.A., Bowen, A.J., Roman, C.W., and Palmiter, R.D. (2018). Encoding of danger by parabrachial CGRP neurons. Nature *555*, 617–622. https://doi.org/10.1038/nature25511.

Cang, Z., and Nie, Q. (2020). Inferring spatial and signaling relationships between cells from single cell transcriptomic data. Nat. Commun. *11*, 2084. https://doi.org/10.1038/s41467-020-15968-5.

Chen, A., Liao, S., Cheng, M., Ma, K., Wu, L., Lai, Y., Qiu, X., Yang, J., Xu, J., Hao, S., et al. (2022). Spatiotemporal transcriptomic atlas of mouse organogenesis using DNA nanoball-patterned arrays. Cell *185*, 1777–1792.e21. https://doi.org/10.1016/j.cell.2022.04.003.

Chen, F., Tillberg, P.W., and Boyden, E.S. (2015). Expansion microscopy. Science *347*, 543–548. https://doi.org/10.1126/science.1260088.

Cho, C.S., Xi, J., Si, Y., Park, S.R., Hsu, J.E., Kim, M., Jun, G., Kang, H.M., and Lee, J.H. (2021). Microscopic examination of spatial transcriptome using Seq-Scope. Cell *184*, 3559–3572.e22. https://doi.org/10.1016/j.cell.2021.05.010.

Codeluppi, S., Borm, L.E., Zeisel, A., La Manno, G., van Lunteren, J.A., Svensson, C.I., and Linnarsson, S. (2018). Spatial organization of the somatosensory cortex revealed by osmFISH. Nat. Methods *15*, 932–935. https://doi.org/10.1038/s41592-018-0175-z.

DeRisi, J., Penland, L., Brown, P.O., Bittner, M.L., Meltzer, P.S., Ray, M., Chen, Y., Su, Y.A., and Trent, J.M. (1996). Use of a cDNA microarray to analyse gene expression patterns in human cancer. Nat. Genet. *14*, 457–460. https://doi.org/10.1038/ng1296-457.

Dobin, A., Davis, C.A., Schlesinger, F., Drenkow, J., Zaleski, C., Jha, S., Batut, P., Chaisson, M., and Gingeras, T.R. (2013). STAR: ultrafast universal RNA-seq aligner. Bioinformatics *29*, 15–21. https://doi.org/10.1093/bioinformatics/bts635.

Dries, R., Zhu, Q., Dong, R., Eng, C.H.L., Li, H., Liu, K., Fu, Y., Zhao, T., Sarkar, A., Bao, F., et al. (2021). Giotto: a toolbox for integrative analysis and visualization of spatial expression data. Genome Biol. *22*, 78. https://doi.org/10.1186/s13059-021-02286-2.

Eng, C.H.L., Lawson, M., Zhu, Q., Dries, R., Koulena, N., Takei, Y., Yun, J., Cronin, C., Karp, C., Yuan, G.C., and Cai, L. (2019). Transcriptome-scale super-resolved imaging in tissues by RNA seqFISH+. Nature *568*, 235–239. https://doi.org/10.1038/s41586-019-1049-y.

Fodor, S.P.A., Read, J.L., Pirrung, M.C., Stryer, L., Lu, A.T., and Solas, D. (1991). Light-directed, spatially addressable parallel chemical synthesis. Science *251*, 767–773. https://doi.org/10.1126/science.1990438.

Gayoso, A., Lopez, R., Xing, G., Boyeau, P., Valiollah Pour Amiri, V., Hong, J., Wu, K., Jayasuriya, M., Mehlman, E., Langevin, M., et al. (2022). A Python library for probabilistic analysis of single-cell omics data. Nat. Biotechnol. *40*, 163–166. https://doi.org/10.1038/s41587-021-01206-w.

Gosselin, D., Skola, D., Coufal, N.G., Holtman, I.R., Schlachetzki, J.C.M., Sajti, E., Jaeger, B.N., O'Connor, C., Fitzpatrick, C., Pasillas, M.P., et al. (2017). An environment-dependent transcriptional network specifies human microglia identity. Science *356*, eaal3222. https://doi.org/10.1126/science.aal3222.

Gu, L., Li, C., Aach, J., Hill, D.E., Vidal, M., and Church, G.M. (2014). Multiplex single-molecule interaction profiling of DNA-barcoded proteins. Nature *515*, 554–557. https://doi.org/10.1038/nature13761.

Hao, Y., Hao, S., Andersen-Nissen, E., Mauck, W.M., Zheng, S., Butler, A., Lee, M.J., Wilk, A.J., Darby, C., Zager, M., et al. (2021). Integrated analysis of multimodal single-cell data. Cell *184*, 3573–3587.e29. https://doi.org/10.1016/j.cell.2021.04.048.

He, Y., Tang, X., Huang, J., Ren, J., Zhou, H., Chen, K., Liu, A., Shi, H., Lin, Z., Li, Q., et al. (2021). ClusterMap: Multi-scale Clustering Analysis of spatial gene expression. Nat. Commun. *12*, 5909. https://doi.org/10.1038/s41467-021-26044-x.

Huang, T., Lin, S.H., Malewicz, N.M., Zhang, Y., Zhang, Y., Goulding, M., LaMotte, R.H., and Ma, Q. (2019). Identifying the pathways required for coping behaviours associated with sustained pain. Nature *565*, 86–90. https://doi.org/10.1038/s41586-018-0793-8.

Jarvie, B.C., Chen, J.Y., King, H.O., and Palmiter, R.D. (2021). Satb2 neurons in the parabrachial nucleus mediate taste perception. Nat. Commun. *12*, 224. https://doi.org/10.1038/s41467-020-20100-8.

Kang, S., Davidsen, K., Gomez-Castillo, L., Jiang, H., Fu, X., Li, Z., Liang, Y., Jahn, M., Moussa, M., DiMaio, F., and Gu, L. (2019). COMBINES-CID: An efficient method for de novo engineering of highly specific chemically induced protein dimerization systems. J. Am. Chem. Soc. *141*, 10948–10952. https://doi.org/10.1021/jacs.9b03522.

Kuleshov, M.V., Jones, M.R., Rouillard, A.D., Fernandez, N.F., Duan, Q., Wang, Z., Koplev, S., Jenkins, S.L., Jagodnik, K.M., Lachmann, A., et al. (2016). Enrichr: a comprehensive gene set enrichment analysis web server 2016 update. Nucleic Acids Res. *44*, W90–W97. https://doi.org/10.1093/nar/gkw377.

Kupari, J., Usoskin, D., Parisien, M., Lou, D., Hu, Y., Fatt, M., Lonnerberg, P., Spangberg, M., Eriksson, B., Barkas, N., et al. (2021). Single cell transcriptomics of primate sensory neurons identifies cell types associated with chronic pain. Nat. Commun. *12*, 1510. https://doi.org/10.1038/s41467-021-21725-z.

Lange, S.A., Benes, V., Kern, D.P., Hörber, J.K.H., and Bernard, A. (2004). Microcontact printing of DNA molecules. Anal. Chem. *76*, 1641–1647. https://doi.org/10.1021/ac035127w.

Langmead, B., Trapnell, C., Pop, M., and Salzberg, S.L. (2009). Ultrafast and memory-efficient alignment of short DNA sequences to the human genome. Genome Biol. *10*, R25. https://doi.org/10.1186/gb-2009-10-3-r25.

Li, Q., Cheng, Z., Zhou, L., Darmanis, S., Neff, N.F., Okamoto, J., Gulati, G., Bennett, M.L., Sun, L.O., Clarke, L.E., et al. (2019). Developmental Heterogeneity of Microglia and Brain Myeloid Cells Revealed by Deep Single-Cell RNA Sequencing. Neuron *101*, 207–223.e10. https://doi.org/10.1016/j.neuron.2018.12.006.

Liddelow, S.A., Guttenplan, K.A., Clarke, L.E., Bennett, F.C., Bohlen, C.J., Schirmer, L., Bennett, M.L., Munch, A.E., Chung, W.S., Peterson, T.C., et al. (2017). Neurotoxic reactive astrocytes are induced by activated microglia. Nature *541*, 481–487. https://doi.org/10.1038/nature21029.

Littman, R., Hemminger, Z., Foreman, R., Arneson, D., Zhang, G., Gómez-Pinilla, F., Yang, X., and Wollman, R. (2021). Joint cell segmentation and cell type annotation for spatial transcriptomics. Mol. Syst. Biol. *17*, e10108. https://doi.org/10.15252/msb.202010108.

Liu, Y., Yang, M., Deng, Y., Su, G., Enninful, A., Guo, C.C., Tebaldi, T., Zhang, D., Kim, D., Bai, Z., et al. (2020). High-spatial-resolution multi-omics sequencing via deterministic barcoding in tissue. Cell *183*, 1665–1681.e18. https://doi.org/10.1016/j.cell.2020.10.026.

Mitra, R., and Church, G.M. (1999). In situ localized amplification and contact replication of many individual DNA molecules. Nucleic Acids Res. *27*, e34. https://doi.org/10.1093/nar/27.24.e34.

Moffitt, J.R., Bambah-Mukku, D., Eichhorn, S.W., Vaughn, E., Shekhar, K., Perez, J.D., Rubinstein, N.D., Hao, J., Regev, A., Dulac, C., and Zhuang, X. (2018). Molecular, spatial, and functional single-cell profiling of the hypothalamic preoptic region. Science *362*, eaau5324. https://doi.org/10.1126/science.aau5324.

Norris, A.J., Shaker, J.R., Cone, A.L., Ndiokho, I.B., and Bruchas, M.R. (2021). Parabrachial opioidergic projections to preoptic hypothalamus mediate behavioral and physiological thermal defenses. Elife *10*, e60779. https://doi.org/10.7554/elife.60779.

Palmiter, R.D. (2018). The Parabrachial Nucleus: CGRP Neurons Function as a General Alarm. Trends Neurosci. *41*, 280–293. https://doi.org/10.1016/j.tins.2018.03.007.

Park, J., Choi, W., Tiesmeyer, S., Long, B., Borm, L.E., Garren, E., Nguyen, T.N., Tasic, B., Codeluppi, S., Graf, T., et al. (2021). Cell segmentation-free inference of cell types from in situ transcriptomics data. Nat. Commun. *12*, 3545. https://doi.org/10.1038/s41467-021-23807-4.

Petukhov, V., Xu, R.J., Soldatov, R.A., Cadinu, P., Khodosevich, K., Moffitt, J.R., and Kharchenko, P.V. (2022). Cell segmentation in imaging-based spatial transcriptomics. Nat. Biotechnol. *40*, 345–354. https://doi.org/10.1038/s41587-021-01044-w.

Pfrieger, F.W., and Ungerer, N. (2011). Cholesterol metabolism in neurons and astrocytes. Prog. Lipid Res. *50*, 357–371. https://doi.org/10.1016/j.plipres.2011.06.002.

Philimonenko, A.A., Janacek, J., and Hozak, P. (2000). Statistical evaluation of colocalization patterns in immunogold labeling experiments. J. Struct. Biol. *132*, 201–210. https://doi.org/10.1006/jsbi.2000.4326.

Pinching, A.J., and Powell, T.P.S. (1971). The Neuron Types of the Glomerular Layer of the Olfactory Bulb. J. Cell Biol. *9*, 305–345. https://doi.org/10.1242/jcs.9.2.305.

Rodriques, S.G., Stickels, R.R., Goeva, A., Martin, C.A., Murray, E., Vanderburg, C.R., Welch, J., Chen, L.M., Chen, F., and Macosko, E.Z. (2019). Slide-seq: A scalable technology for measuring genome-wide expression at high spatial resolution. Science *363*, 1463–1467. https://doi.org/10.1126/science.aaw1219.

Roehr, J.T., Dieterich, C., and Reinert, K. (2017). Flexbar 3.0-SIMD and multicore parallelization. Bioinformatics *33*, 2941–2942. https://doi.org/10.1093/bioinformatics/btx330.

Schena, M., Shalon, D., Davis, R.W., and Brown, P.O. (1995). Quantitative monitoring of gene expression patterns with a complementary DNA microarray. Science *270*, 467–470. https://doi.org/10.1126/science.270.5235.467.

Seltzer, Z., Dubner, R., and Shir, Y. (1990). A novel behavioral model of neuropathic pain disorders produced in rats by partial sciatic nerve injury. Pain *43*, 205–218. https://doi.org/10.1016/0304-3959(90)91074-s.

Stahl, P.L., Salmen, F., Vickovic, S., Lundmark, A., Navarro, J.F., Magnusson, J., Giacomello, S., Asp, M., Westholm, J.O., Huss, M., et al. (2016). Visualization and analysis of gene expression in tissue sections by spatial transcriptomics. Science *353*, 78–82. https://doi.org/10.1126/science.aaf2403.

Stickels, R.R., Murray, E., Kumar, P., Li, J., Marshall, J.L., Di Bella, D.J., Arlotta, P., Macosko, E.Z., and Chen, F. (2021). Highly sensitive spatial transcriptomics at near-cellular resolution with Slide-seqV2. Nat. Biotechnol. *39*, 313–319. https://doi.org/10.1038/s41587-020-0739-1.

Street, K., Risso, D., Fletcher, R.B., Das, D., Ngai, J., Yosef, N., Purdom, E., and Dudoit, S. (2018). Slingshot: cell lineage and pseudotime inference for single-cell transcriptomics. BMC Genom. *19*, 477. https://doi.org/10.1186/s12864-018-4772-0.

Stringer, C., Wang, T., Michaelos, M., and Pachitariu, M. (2021). Cellpose: a generalist algorithm for cellular segmentation. Nat. Methods *18*, 100–106. https://doi.org/10.1038/s41592-020-01018-x.

Sun, L., Liu, R., Guo, F., Wen, M.Q., Ma, X.L., Li, K.Y., Sun, H., Xu, C.L., Li, Y.Y., Wu, M.Y., et al. (2020). Parabrachial nucleus circuit governs neuropathic pain-like behavior. Nat. Commun. *11*, 5974. https://doi.org/10.1038/s41467-020-19767-w.

Tepe, B., Hill, M.C., Pekarek, B.T., Hunt, P.J., Martin, T.J., Martin, J.F., and Arenkiel, B.R. (2018). Single-cell RNA-seq of mouse olfactory bulb reveals cellular heterogeneity and activity-dependent molecular census of adult-born neurons. Cell Rep. *25*, 2689–2703.e3. https://doi.org/10.1016/j.celrep.2018.11.034.

Vainchtein, I.D., and Molofsky, A.V. (2020). Astrocytes and Microglia: In Sickness and in Health. Trends Neurosci. *43*, 144–154. https://doi.org/10.1016/j.tins.2020.01.003.

Vickovic, S., Eraslan, G., Salmen, F., Klughammer, J., Stenbeck, L., Schapiro, D., Aijo, T., Bonneau, R., Bergenstrahle, L., Navarro, J.F., et al. (2019). High-definition spatial transcriptomics for in situ tissue profiling. Nat. Methods *16*, 987–990. https://doi.org/10.1038/s41592-019-0548-y.

Vickovic, S., Lotstedt, B., Klughammer, J., Mages, S., Segerstolpe, A., Rozenblatt-Rosen, O., and Regev, A. (2022). SM-Omics is an automated platform for high-throughput spatial multi-omics. Nat. Commun. *13*, 795. https://doi.org/10.1038/s41467-022-28445-y.

Wang, B., Wan, L., Wang, A., and Li, L.M. (2017). An adaptive decorrelation method removes Illumina DNA base-calling errors caused by crosstalk between adjacent clusters. Sci. Rep. *7*, 41348. https://doi.org/10.1038/srep41348.

Xia, Y., and Whitesides, G.M. (1998). Soft lithography. Angew. Chem. Int. Ed. Engl. *37*, 550–575. https://doi.org/10.1002/(sici)1521-3773(19980316)37:5<550::aid-anie550>3.0.co;2-g.

Yap, E.L., and Greenberg, M.E. (2018). Activity-Regulated Transcription: Bridging the Gap between Neural Activity and Behavior. Neuron *100*, 330–348. https://doi.org/10.1016/j.neuron.2018.10.013.

Zeisel, A., Hochgerner, H., Lonnerberg, P., Johnsson, A., Memic, F., van der Zwan, J., Haring, M., Braun, E., Borm, L.E., La Manno, G., et al. (2018). Molecular architecture of the mouse nervous system. Cell *174*, 999–1014.e22. https://doi.org/10.1016/j.cell.2018.06.021.

Zhao, J., Jaffe, A., Li, H., Lindenbaum, O., Sefik, E., Jackson, R., Cheng, X., Flavell, R.A., and Kluger, Y. (2021). Detection of differentially abundant cell subpopulations in scRNA-seq data. Proc. Natl. Acad. Sci. USA. *118*, e2100293118. https://doi.org/10.1073/pnas.2100293118.